Applied Catalysis B: Environmental 125 (2012) 11–20

Contents lists available at SciVerse ScienceDirect

Applied Catalysis B: Environmental

journal homepage: www.elsevier.com/locate/apcatb

Novel mesoporous $Zn_xCd_{1-x}S$ nanoparticles as highly efficient photocatalysts

Xin Xu, Ruijuan Lu, Xiaofei Zhao, Yue Zhu, Sailong Xu, Fazhi Zhang*

State Key Laboratory of Chemical Resource Engineering, Beijing University of Chemical Technology, Beijing 100029, China

ARTICLE INFO

Article history:
Received 22 February 2012
Received in revised form 17 May 2012
Accepted 20 May 2012
Available online 27 May 2012

Keywords:
CdS
Layered double hydroxide
Photocatalysis
Mesoporous

ABSTRACT

Porous semiconductor photocatalysts which are active under illumination by visible light have attracted extensive attention recently due to their remarkable well-designed physical and chemical properties. Here, novel mesoporous $Zn_xCd_{1-x}S$ nanoparticles have been successfully fabricated by a two-steps strategy: Al-$Zn_xCd_{1-x}S$ nanoparticles which are homogeneously distributed within the confinement of an amorphous alumina matrix was first synthesized by *in situ* gas–solid reaction of a single precursor—a Zn^{2+},Cd^{2+},Al^{3+}-containing layered double hydroxides (ZnCdAl-LDHs)—with gaseous H_2S; subsequently, selective leaching of amorphous alumina by sodium hydroxide solution from the as-prepared Al-$Zn_xCd_{1-x}S$ nanoparticles was carried out, with the aim of achieving the introduction of mesopority in the chalcogenide semiconductor. The resulting mesoporous $Zn_xCd_{1-x}S$ nanoparticles can retain the uniform distributed structure with a network-like manner after the selective leaching of amorphous alumina. The absorption edge of the mesoporous $Zn_xCd_{1-x}S$ exhibit a monotonic blue shift within the visible light region as the amount of residual alumina decreased. The photocatalytic activities of the mesoporous $Zn_xCd_{1-x}S$ samples for the photodegradation of methylene blue (MB) dye molecules increase with the decline of alumina. And, the mesoporous $Zn_xCd_{1-x}S$ exhibits an enhanced photocatalytic performance compared to the pure CdS sample obtained from the same procedure without Zn^{2+}, the unleached Al-$Zn_xCd_{1-x}S$ sample and the sample obtained by a coprecipitation method with the same composition. The homogeneous structure of the mesoporous $Zn_xCd_{1-x}S$ and the abundant surface hydroxyl groups are proposed to be beneficial to the generation of hydroxyl radicals, identified by electron spin resonance (ESR) spectra, leading to the higher photocatalytic activity.

1. Introduction

Environmental problems associated with organic pollutants and toxic water pollutants provide the impetus for sustained fundamental and applied research in the area of environmental remediation. A number of remarkable progresses of semiconductor photocatalysis have been achieved in environmental pollution degradation in the past decade [1–3]. Porous photocatalysts with well-designed physical and chemical properties, such as high surface area to facilitate the diffusion of reactants and more active sites for carrying out catalytic reactions, provide a model system for investigating and understanding the dependence of photocatalytic performance on materials composition and structure at various scales, as well as for fundamental studies of reaction mechanism and kinetics [4]. Such understandings in turn will greatly promote a better design of highly efficient photocatalysts. Enormous efforts have been devoted to developing the fabrication techniques for the porous semiconductors to enhance the photocatalytic activity, for example the template method [5–7], the self-organization method [8,9], the etching route [10,11], and the topotactic transition [12].

As a typical solid solution semiconductor, $Zn_xCd_{1-x}S$ has been intensively investigated because it has good and tunable absorption properties in the visible region of the solar spectrum, excellent electrical conductivity and valence bands at relatively negative potentials [13–15], allowing $Zn_xCd_{1-x}S$ having good visible-light-driven photocatalytic activity in H_2 evolution from water [16,17] and the decomposition of organic compounds [18–20]. In our previous work [21], $Zn_xCd_{1-x}S$ solid solution was prepared through an *in situ* gas–solid sulfuration reaction of a single layered double hydroxides (LDHs) precursor with H_2S, by taking advantage of the attractive feature of LDHs chemistry *viz.* the homogenous distribution of the different metal cations within the layers on an atomic level [22]. The resulting $Zn_xCd_{1-x}S$ exhibited significantly better photocatalytic performance for the degradation of methylene blue (MB) molecules than $Zn_xCd_{1-x}S$ with the same composition obtained either by a coprecipitation method or by sulfuration of a physical mixture of ZnAl-LDHs and CdAl-LDHs precursor, which may be resulted from a homogeneous distributed structure of the $Zn_xCd_{1-x}S$ solid solution, suppressing the recombination of photoexcited electrons and holes.

* Corresponding author. Fax: +86 10 6442 5385.
E-mail address: zhangfz@mail.buct.edu.cn (F. Zhang).

0926-3373/$ – see front matter © 2012 Elsevier B.V. All rights reserved.
http://dx.doi.org/10.1016/j.apcatb.2012.05.018

LDHs are a family of anionic clays that can be described by the general formula $[M^{2+}_{1-x}M^{3+}_{x}(OH)_2]^{x+}A^{n-}_{x/n}\cdot mH_2O$, where M^{2+} and M^{3+} are di-and tri-valent cations, respectively; the value of the coefficient x is equal to the molar ratio of $M^{3+}/(M^{2+}+M^{3+})$; and A^{n-} is an anion [23–25]. A large class of isostructural materials can be obtained by changing the metal cations, the molar ratio M^{2+}/M^{3+}, or the interlayer anions. LDHs containing three or even more cations in the layers can also be prepared. This flexibility in composition allows LDHs with a wide variety of properties to be prepared and is one of their most attractive features [26]. In this paper, with the aim of achieving the introduction of mesopority in the chalcogenide semiconductor and improving the photocatalytic activity, we propose a two-steps strategy to obtain mesoporous $Zn_xCd_{1-x}S$ material: Al-$Zn_xCd_{1-x}S$ nanoparticles which are homogeneously distributed within the confinement of an amorphous alumina matrix were first synthesized by *in situ* gas–solid reaction of a single ZnCdAl-LDHs precursor with gaseous H_2S; subsequently, selective leaching of amorphous alumina by sodium hydroxide solution from the main layers of the as-prepared Al-$Zn_xCd_{1-x}S$ nanoparticles was carried out. The fabrication process is illustrated schematically in Fig. 1. The chalcogenide semiconductor before and after leaching are characterized by X-ray diffraction (XRD), N_2 adsorption measurements, ultraviolet–visible spectroscopy (UV–vis), scanning electron microscope (SEM), transmission electron microscopy (TEM), X-ray photo electron spectroscopy (XPS), and solid-state magic-angle spinning nuclear magnetic resonance (MAS NMR) techniques. Furthermore, the photocatalyic performances of the resulting mesoporous $Zn_xCd_{1-x}S$ samples, as well as the unleached sample and the sample obtained by a coprecipitation method with the same composition, for the degradation of MB dye molecules under visible light irradiation ($\lambda \geq 420$ nm) are investigated systematically. Electron spin resonance (ESR) spectra of paramagnetic species spin-trapped with 5,5-dimethylpyrroline-*N*-oxide (DMPO) were recorded in order to measure the formation of active radical species during irradiation of the dye dispersion for the different photocatalyst samples. Our method provides a way to fabricate new types of visible-light response mesoporous chalcogenide semiconductor photocatalysts with uniform distributed structure.

2. Experimental

2.1. Materials preparation

The Al-$Zn_xCd_{1-x}S$ solid solution was prepared by *in situ* gas–solid sulfuration reaction between ZnCdAl-LDHs precursor and gaseous H_2S [21]. All reagents were commercially available and used as received without further purification. Typically, for the synthesis of ZnCdAl-LDHs with Zn/Cd/Al molar ratio of 1/2/1, a $Zn(NO_3)_2\cdot 9H_2O$ solution (0.01 mol), $Cd(NO_3)_2\cdot 4H_2O$ (0.02 mol), and $Al(NO_3)_3\cdot 9H_2O$ (0.01 mol) (with a total M^{2+}/M^{3+} molar ratio of 3/1) in decarbonated H_2O (15.8 mL) was mixed with a solution of dodecyl sulfate (DS) surfactant (85 mL, 0.24 M). A NaOH solution (2 M) was then added dropwise to the resulting solution until a pH of 8.0 was attained, and the system was then aged at room temperature for 6 h. The solid product was separated by centrifugation, washed with decarbonated water and then alcohol. The resulting sample, denoted Al-$Zn_{0.33}Cd_{0.67}S$, was finally dried under vacuum. ZnCdAl-LDHs precursor compounds with Zn/Cd/Al molar ratios of 0.6/2.4/1 and 2/1/1, retaining a total M^{2+}/M^{3+} molar ratio of 3/1, were synthesized under the same reaction conditions, and are denoted Al-$Zn_{0.20}Cd_{0.80}S$ and Al-$Zn_{0.67}Cd_{0.33}S$, respectively. To leach the alumina, the Al-$Zn_xCd_{1-x}S$ samples (1.0 g) were subsequently treated with 30 mL of aqueous sodium hydroxide solution (10 M) at different temperature for 48 h under moderate stirring. The final products were separated by centrifugation, separately

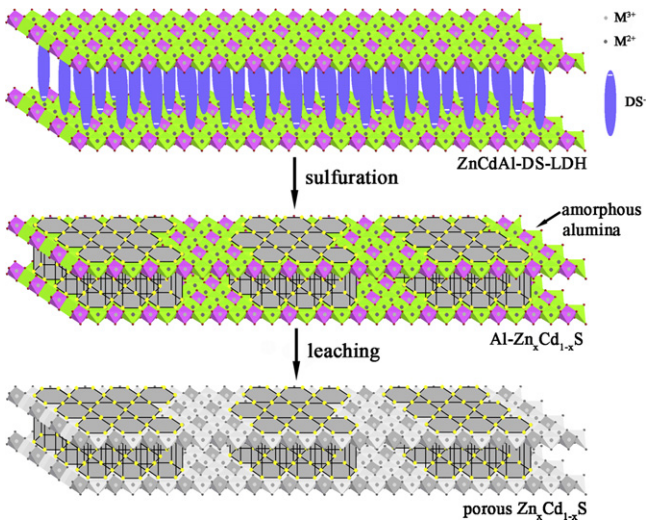

Fig. 1. Schematic illustration of the preparation of mesoporous $Zn_xCd_{1-x}S$ solid solution.

washed with decarbonated water and alcohol several times until pH 7, and finally dried at 60 °C overnight. Al-$Zn_xCd_{1-x}S$ samples were leached at 30, 40, 50 and 60 °C are denoted $Zn_xCd_{1-x}S$-30, $Zn_xCd_{1-x}S$-40, $Zn_xCd_{1-x}S$-50 and $Zn_xCd_{1-x}S$-60, respectively.

For comparison, the coprecipitation method [18] was used to prepare a sample of $Zn_xCd_{1-x}S$. In brief, an appropriate amount of analytical grade $Zn(OAc)_2\cdot 2H_2O$ (OAc = acetate) and $Cd(OAc)_2\cdot 2H_2O$ with Zn/Cd molar ratio of 1/4, were dissolved in deionized water to form a 0.434 M solution. Then Na_2S solution (0.5 M) was slowly added dropwise to the mixture with continuous stirring. The procedure was carried out in a Teflon-lined 100 mL container. After being stirred for 12 h at room temperature, the Teflon-lined container was then sealed in a stainless steel autoclave and maintained at 160 °C for 24 h. Finally, the autoclave was allowed to cool to ambient temperature, and the resulting product was washed several times with water/ethanol and then dried in vacuum at 60 °C for 3 h. The sample is denoted $Zn_{0.20}Cd_{0.80}S$-cp. Additionally, the pure CdS sample obtained from the same procedure without Zn^{2+}, which is denoted CdS-40 as the leaching temperature was 40 °C.

2.2. Characterization

XRD patterns of the products were recorded on a Shimadzu XRD-6000 diffractometer, using Cu Kα radiation ($\lambda = 0.15418$ nm) at 40 kV and 30 mA. FT-IR spectra were recorded using KBr discs in the region 400–4000 cm^{-1} with a Bruker Vector 22 spectrometer. SEM images were obtained using a Hitachi S-4700 field emission SEM at 20 kV, with the surface of the samples coated with a thin platinum layer to avoid a charging effect. TEM images were recorded on a JEOL JEM-2010 high-resolution transmission electron microscope at an accelerating voltage of 200 kV. The sample was ultrasonically dispersed in ethanol, and then the suspension was deposited on a microgrid coated with a holey carbon film. UV–vis diffuse reflectance spectra were recorded at room temperature in air on a Shimadzu UV-2501PC spectrometer equipped with an integrating sphere attachment using $BaSO_4$ as background. Elemental analyses for metals were performed with a Shimadzu ICPS-7500 inductively coupled plasma emission spectrometer on solutions prepared by dissolving the samples in dilute HNO_3, and sulfur content was analyzed using a Kaiyuan 5E-8SII sulfur analyzer. XPS were recorded with a PHIQ2000 X-ray photoelectron spectrometer equipped with a monochromatized Al Kα X-ray source. An operating power of

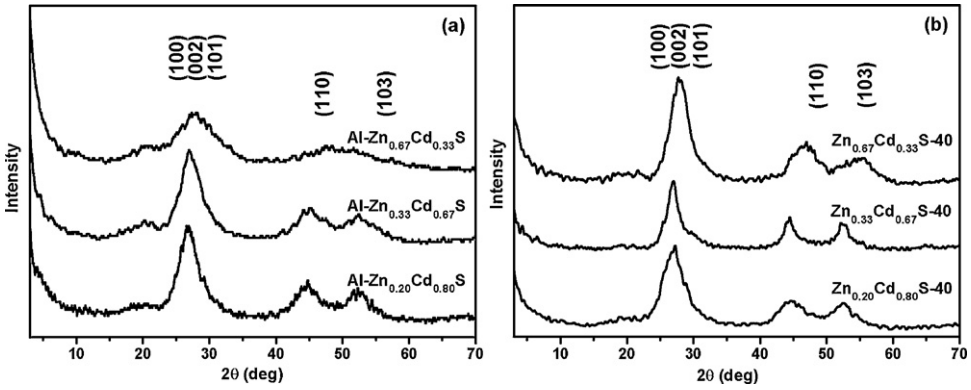

Fig. 2. XRD patterns of samples with different Zn/Cd mole ratio before (a) and after (b) NaOH leaching at 40 °C.

25 W was used with a spot diameter of 100 μm. ^{27}Al solid-state MAS NMR spectra were measured on a Bruker AV300 spectrometer operating at 78.20 MHz with a pulse width of 0.5 s, spinning rate of 8000 Hz, and an acquisition delay of 0.5 μs between successive pulses to avoid saturation effects. The specific surface area determination and pore volume and size analysis were performed by BET and BJH methods, with nitrogen adsorption at 77 K using a Quantachrome Autosorb-1C-VP Analyzer. Prior to the measurements, samples were degassed at 120 °C for 2 h. ESR spectra of paramagnetic species spin-trapped with DMPO were recorded with a Bruker EPR 300E spectrometer in order to measure the formation of active radical species during irradiation of the dye dispersion (1×10^{-5} M) containing 2 mg of catalyst particles; the irradiation source (λ = 532 nm) was a Quanta-Ray Nd:YAG pulsed (10 pulses per second) laser system.

2.3. Photocatalytic activity measurement

Photocatalytic activities of the resulting samples were evaluated using the photodegradation of MB molecules under visible light irradiation as a model reaction. The apparatus for the photocatalytic experiments was shown in Fig. S1 (see the Electronic Supplementary Information). A quartz beaker (capacity 150 mL) was used as the photoreaction vessel. Typically, the reaction system containing MB (aqueous solution, 1×10^{-5} M, 100 mL) and the mesoporous $Zn_xCd_{1-x}S$ sample (30 mg) was magnetically stirred in the dark for 30 min to reach the adsorption equilibrium of MB with the sample and was then exposed to light from a 300 W Xe lamp equipped with a UV cutoff filter (λ ≥ 420 nm). The spectral emission of the lamp source was shown in the Fig. S2. The path length between the lamp and the quartz beaker is 52 cm, which keeps the light intensity on the quartz beaker is 100 mw/cm^2. At specific time intervals, 3 mL of the reaction solution was withdrawn by a syringe. The reactor's temperature was monitored by the thermometer to ensure that the reaction system kept room temperature during the whole process. The solution was centrifuged to remove the sample before being analyzed by UV–vis absorption spectroscopy. A blank reaction was carried out following the same procedure without adding any catalyst sample.

3. Results and discussion

The solid solution which is homogeneously distributed within the confinement of an amorphous alumina matrix was first prepared through *in situ* gas–solid sulfuration reaction of a single ZnCdAl-LDHs precursor with H_2S. When the Al-$Zn_xCd_{1-x}S$ samples with different Zn/Cd molar ratio were subsequently leached by NaOH solution, their original yellow color deepened at different degrees: the intensity of the yellow color deepened with the decrease of the Zn mole fraction (*i.e.*, the decrease of the value of *x*). Fig. 2 shows the XRD patterns of the $Zn_xCd_{1-x}S$ samples before and after treatment with alkali at 40 °C. As shown in Fig. 2a, the broad peaks which can be indexed to the (1 1 0), (1 0 3) and overlapping (1 0 0), (0 0 2), and (1 0 1) reflections of a hexagonal metal sulfide of the $Cd_{0.80}Zn_{0.20}S$ (JCPDF No. 491302) was observed. Meanwhile, the patterns of the leached samples exhibit the characteristic reflections of $Zn_xCd_{1-x}S$ solid solution with stronger reflection intensities (Fig. 2b). It is demonstrated that the $Zn_xCd_{1-x}S$ structure can be retained during the leaching process, and the crystallinity has been improved. In addition, the diffraction peaks shift to larger angles as the Zn mole fraction increase.

Table 1 summarizes the chemical compositions of the $Zn_xCd_{1-x}S$ samples before and after NaOH leaching at 40 and 50 °C. The Zn/Cd molar ratios in $Zn_{0.20}Cd_{0.80}S$-40, $Zn_{0.33}Cd_{0.67}S$-40 and $Zn_{0.67}Cd_{0.33}S$-40 are essentially identical to those corresponding unleached Al-$Zn_xCd_{1-x}S$ samples. While the Zn/Cd molar ratios in $Zn_{0.20}Cd_{0.80}S$-50 decrease obviously, suggesting that partial loss of Zn^{2+} at higher treatment temperature. The M^{2+}/M^{3+} molar ratios in the three leached -40 samples are 10.6, 10.8 and 10.9, respectively, which was much more than the value of the unleached samples, suggesting the effective removal of amorphous alumina. Moreover, with the increase of the treating temperature to 50 °C, the M^{2+}/M^{3+} molar ratios in the -50 sample increase to 12.7. On the other hand, the measured S/M^{2+} molar ratios are very close to 1.0, suggesting that the S atoms in the $Zn_xCd_{1-x}S$ samples can be retained during the leaching process. Further, Fig. 3 shows that the lattice parameter *c* measured from the XRD patterns of the $Zn_xCd_{1-x}S$ materials, which exhibits a nearly linear relationship with the Zn mole fraction. A gradual decrease in lattice parameter *c* was observed as the Zn mole fraction (*x*) increases. This is consistent with Vegard's law, and indicates that a homogeneous solid solution structure rather than physical mixture has been formed [27,28].

Table 1
Chemical composition of samples with different Zn/Cd mole ratio before and after NaOH leaching.

Sample	Zn/Cd ratio[a]	M^{2+}/M^{3+} ratio[a]	S/M^{2+} ratio[b]
Al-$Zn_{0.20}Cd_{0.80}S$	0.25	2.94	0.996
Al-$Zn_{0.33}Cd_{0.67}S$	0.51	2.97	0.995
Al-$Zn_{0.67}Cd_{0.33}S$	2.06	3.02	0.997
$Zn_{0.20}Cd_{0.80}S$-40	0.22	10.6	0.997
$Zn_{0.33}Cd_{0.67}S$-40	0.47	10.8	0.994
$Zn_{0.67}Cd_{0.33}S$-40	2.01	10.9	0.996
$Zn_{0.20}Cd_{0.80}S$-50	0.16	12.7	0.993
Coprecipitation $Zn_{0.20}Cd_{0.80}S$	0.23	/	0.995

[a] Amounts of M^{2+} and M^{3+} determined by ICP.
[b] Amount of S determined by elemental analysis.

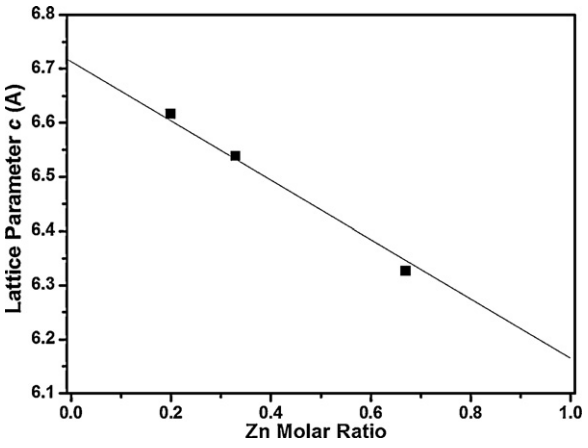

Fig. 3. Variation of the lattice parameter c of $Zn_xCd_{1-x}S$ with Zn mole fraction. (■ are experimental data points and the line shows a Vegard's law plot of the c lattice parameter.).

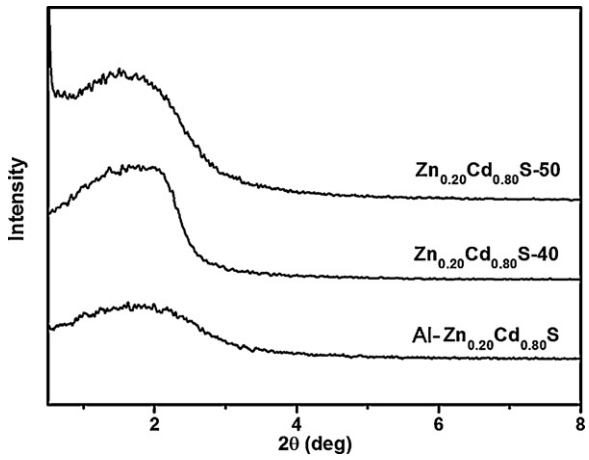

Fig. 4. Low-angle XRD patterns of $Zn_{0.20}Cd_{0.80}S$ before and after NaOH leaching at 40–50 °C.

Additionally, the low-angle XRD patterns of the mesoporous $Zn_xCd_{1-x}S$ solid solution before and after NaOH leaching (Fig. 4) show a single reflection in the low-angle region below 2°, which is characteristic of disordered mesostructures [29,30]. It is demonstrated that the samples before and after leaching treatment are short-range order and long-range disorder mesoporous materials. It is reported that a slight broadening of the peak indicates a certain degree of loss in structural order [31,32]. Therefore, the ordered mesostructure for the $Zn_xCd_{1-x}S$ solid solution is improved after NaOH leaching treatment.

Fig. 5 reveals the structural features of $Zn_xCd_{1-x}S$ before and after leaching, using $Zn_{0.20}Cd_{0.80}S$ as a representative sample. Before NaOH leaching, both $Zn_{0.20}Cd_{0.80}S$ nanoparticles and the amorphous alumina can be seen, and they are woven within each

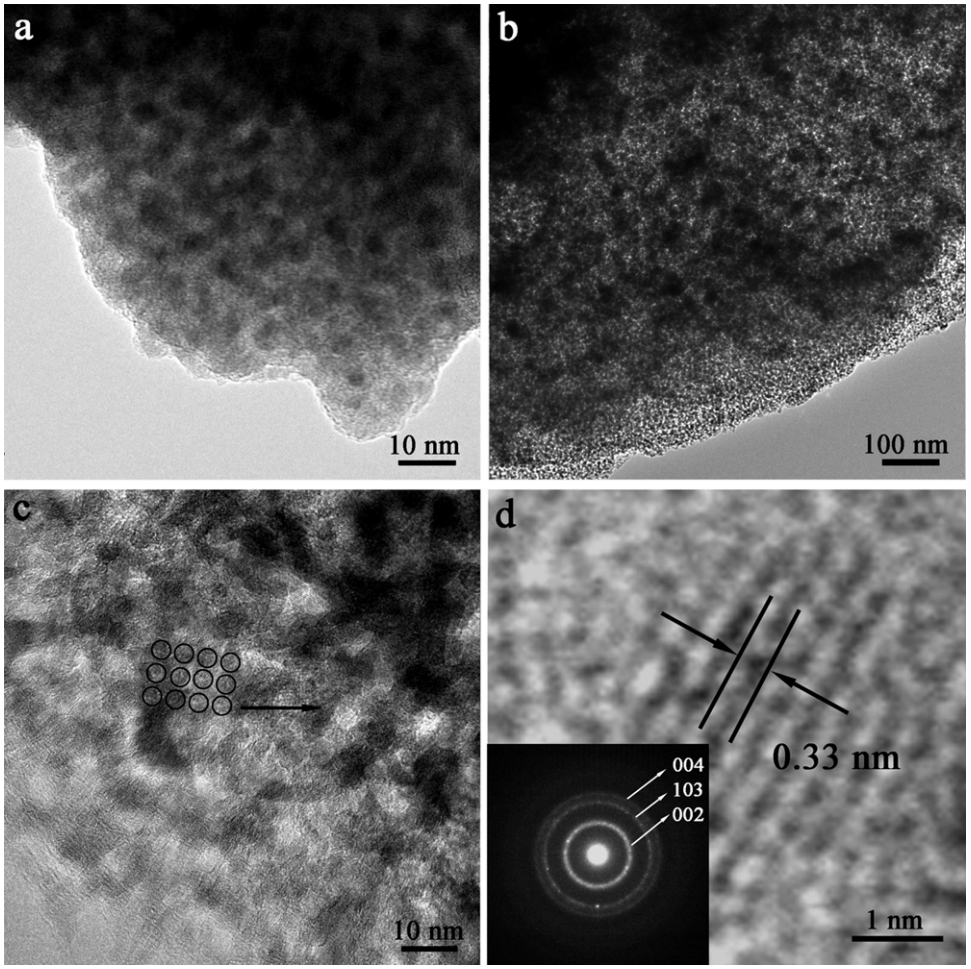

Fig. 5. HRTEM images of $Zn_{0.20}Cd_{0.80}S$ before (a) and (b) after NaOH leaching at 40 °C. (c) and (d) show high magnification views of (b), and the inset in (d) is the selected area electron diffraction pattern.

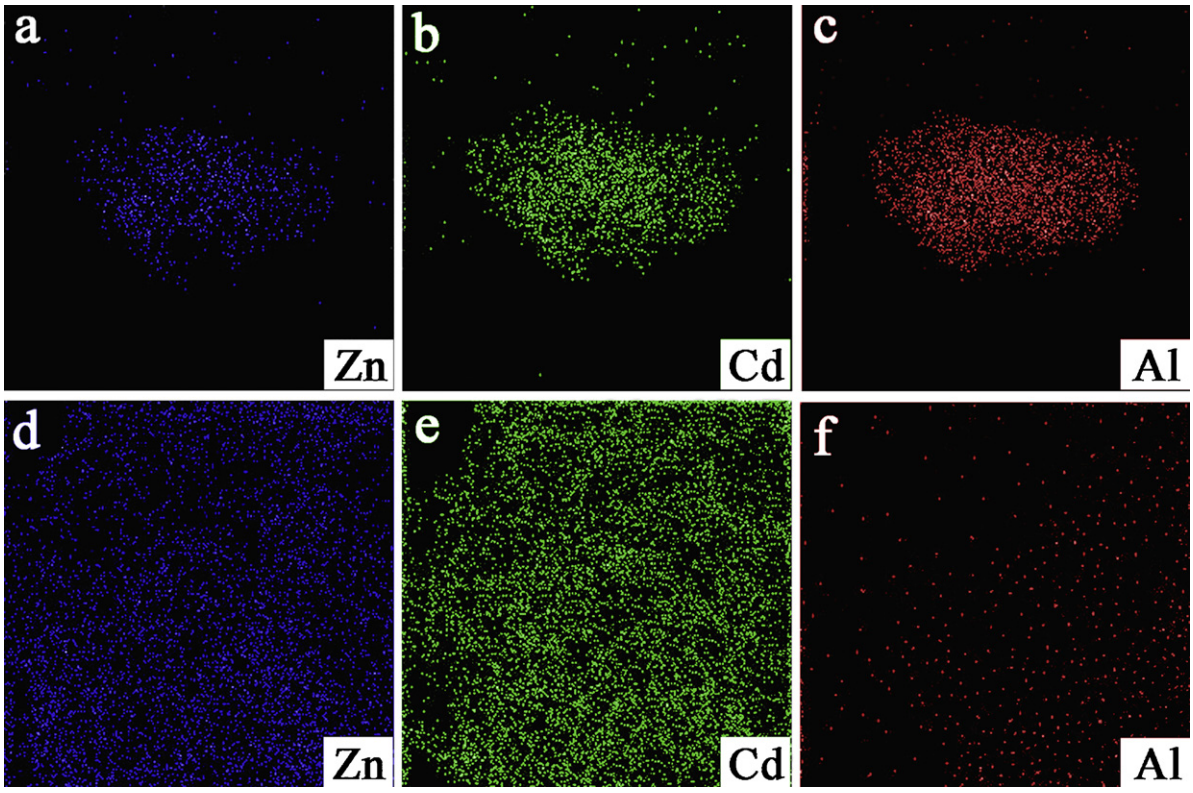

Fig. 6. Zinc, cadmium and aluminum elemental maps using EELS of $Zn_{0.20}Cd_{0.80}S$ before (a, b, c) and after (d, e, f) NaOH leaching at 40 °C.

other (Fig. 5a). This suggests that the formation of $Zn_{0.20}Cd_{0.80}S$ nanoparticles occurs throughout an alumina matrix (the bright region) during the sulfuration reaction [33]. The nanoparticles are arranged regularly to form an uniform distributed structure and the particle diameter, with a mean value of 3.0–4.0 nm (as indicated by black dots), is confined by the segregation and growth-inhibiting effects of the alumina matrix. After NaOH leaching at 40 °C, the $Zn_{0.20}Cd_{0.80}S$-40 nanoparticles retain the uniform structure with a network-like manner (Fig. 5b and c). And, the contrast of TEM image increase distinctly. The lattice fringe of $Zn_{0.20}Cd_{0.80}S$-40 with the interlayer spacing of about 0.33 nm (Fig. 3d) corresponds to the (0 0 2) reflection of $Cd_{0.80}Zn_{0.20}S$ (JCPDF No. 491302). In the selected area electron diffraction pattern (Fig. 3d, inset), and the diffraction rings/spots were observed that can be indexed to the (0 0 2), (1 0 3) and (0 0 4) reflections of a hexagonal $Zn_xCd_{1-x}S$ phase, which was confirming the $Zn_{0.20}Cd_{0.80}S$-40 structure can be preserved during the selective leaching process.

Fig. 6 shows the zinc, cadmium and aluminum elemental electron energy loss spectroscopy (EELS) maps of $Zn_xCd_{1-x}S$ samples before and after leaching. The Zn, Cd and Al elements are consistently distributed in the unleached $Zn_xCd_{1-x}S$ sample (Fig. 6a–c). After NaOH leaching, the Zn and Cd elements in -40 sample can keep their distribution in a uniform manner, and the concentrations are similar to that in the untreated sample. However, it is obvious that the Al concentrations reduce in the leached sample, suggesting the successful removal of the amorphous alumina. The above results are coincident with the ICP analysis (Table 1).

To better understand the detailed structure and surface state of $Zn_xCd_{1-x}S$ samples before and after leaching, the XPS studies were carried out. As shown in Fig. 7a and b, the XPS spectra of $Zn_{0.20}Cd_{0.80}S$ show peaks due to Zn $2p_{3/2}$ and Cd $3d_{5/2}$ at approximately 1021.6 eV and 405.3 eV, respectively, matching well with the reported values for $Zn_xCd_{1-x}S$ solid solution [34]. Moreover, we observed a regular decrease in the binding energy (BE) of Zn $2p_{3/2}$ and Cd $3d_{5/2}$ with the increasing leaching temperature. This may be due to that with the increasing of leaching temperature more alumina was removed. It is inferred that the system is more similar to pure ZnCdS[35], which has a lower BE of both Zn 2p and Cd 3d and a more stable status. No changes are, however, observed in the symmetry of the two peaks (Fig. 7a and b), consistent with the results in the literature [35]. As shown in Fig. 7c, the intensity of the Al characteristic peak located at 75.3 eV decreases sharply after NaOH leaching. And, this characteristic peak disappears for the sample with a higher leaching temperature 50 °C, indicating the removal of the alumina. The XPS spectra of the S $2p_{3/2}$ at around 162 eV (Fig. 7d) are in good agreement with the reported values [36,37] for $Zn_xCd_{1-x}S$. As can be seen in Fig. 7e, the O 1s region is composed of two peaks. The main contribution is attributed to S—O in $-SO_4^{2-}$, and the other at around 530 eV is the hydroxyl group [38]. The hydroxyl content in the two samples after alkali treatment is greater than that before treatment, and the content in -40 sample is the most among the three samples. After selective leaching, a large number of dangling bonds are generated on the surface of the residual alumina, and then some adsorbed H_2O can react with residual alumina to form Al—OH, such as, $H_2O + Al—O—Al \rightarrow 2\ Al—OH$ [39]. Accordingly, the leaching condition must be well controlled to guarantee the proper amount of the residual alumina, and the excessive leaching may hinder hydroxyl group generation. Hydroxyl group existed in the samples is attributable to the chemically adsorbed H_2O. Although some H_2O is physically adsorbed on the surface of the treated samples, the physically adsorbed H_2O is easily desorbed under the ultra-high vacuum condition of the XPS system. Therefore, the XPS spectra do not show the physically adsorbed H_2O on samples.

To better elucidate the leaching process at different temperature, ^{27}Al MAS NMR studies of the $Zn_xCd_{1-x}S$ before and after NaOH leaching, as well as the ZnCdAl-LDHs precursor, were undertaken. As shown in Fig. 8a, the ^{27}Al MAS NMR of the ZnCdAl-LDHs

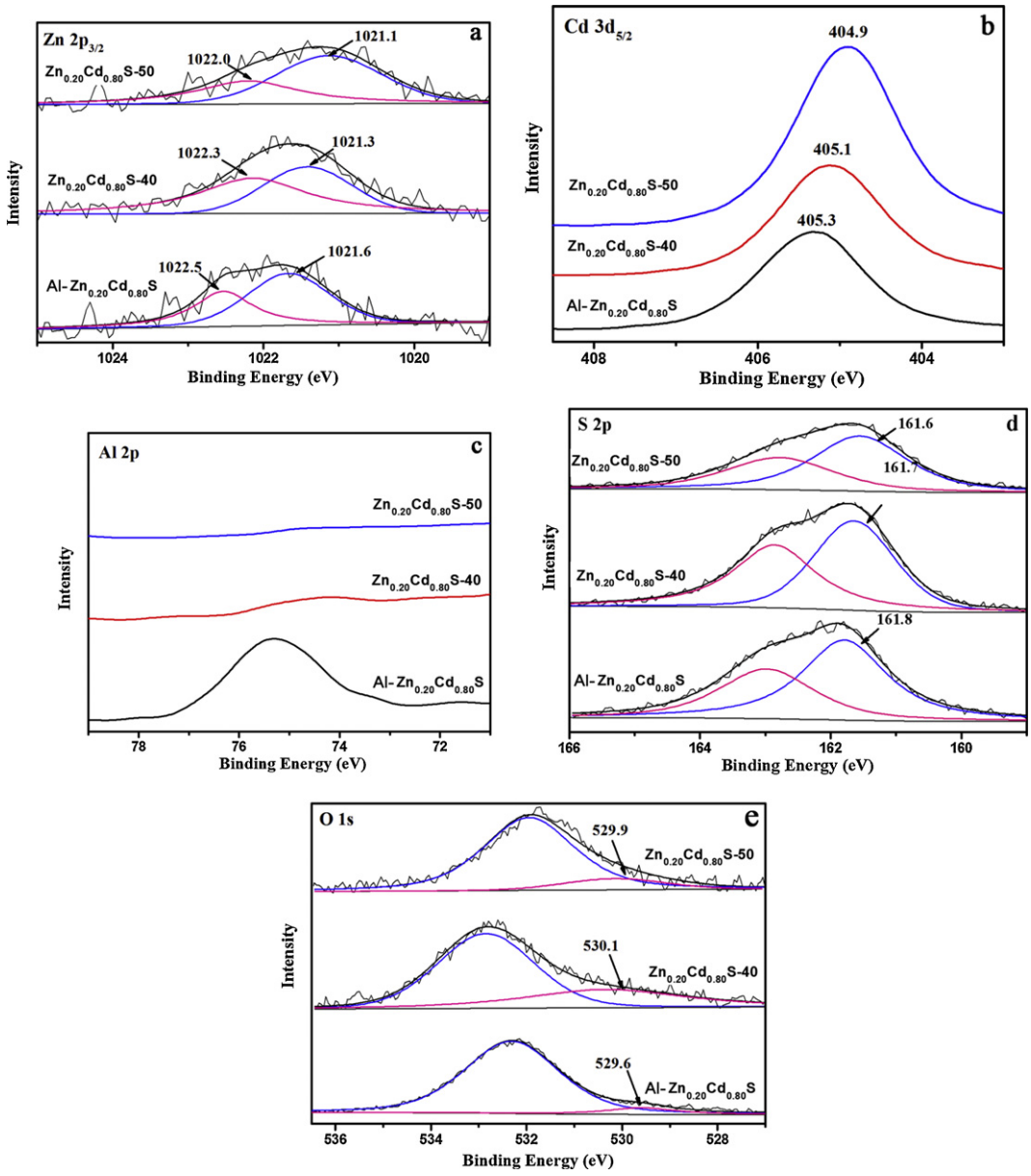

Fig. 7. XPS spectra of $Zn_{0.20}Cd_{0.80}S$ before and after NaOH leaching at 40 °C and 50 °C: (a) Zn 2p, (b) Cd 3d, (c) Al 2p, (d) S 2p, and (e) O 1s.

sample indicates the unique presence of octahedral aluminum at $\delta \sim 7$–14 ppm [40]. During the sulfuration process, the Al^{3+} cations migrate into the gallery space to form amorphous alumina and adopt a octahedral coordination at $\delta \sim -20$–0 ppm (Fig. 8b) [41], in marked contrast to the aggregation that occurs with $Zn_xCd_{1-x}S$ nanoparticles, the distribution of element and crystal structure is not damaged. Some negative shift is observed which is attributed to the change of chemical environment around. After the leaching reaction at 40 °C, the Al^{3+} in the residual aluminum showed evidence of pentahedral coordination at $\delta \sim 20$–45 ppm [41] in the spectrum of the $Zn_{0.20}Cd_{0.80}S$-40 sample (Fig. 8c). Raising the treatment temperature to 50 °C, a new tetrahedral coordinated Al species at $\delta \sim 45$–80 ppm can be found in the $Zn_{0.20}Cd_{0.80}S$-50 sample, indicating that the sample become more stable after sufficient alkali treatment.

To further investigate the segregation and growth-inhibiting effects of the alumina matrix and obtain detailed information about the textural properties before and after removal of amorphous alumina, the samples were analyzed by nitrogen adsorption measurements. Fig. 9a shows the nitrogen adsorption isotherms of the $Zn_xCd_{1-x}S$ before and after NaOH leaching. The pore size distributions (Fig. 9b) were determined by means of the Barrett–Joyner–Halenda (BJH) model from the desorption branches of the nitrogen adsorption isotherms. The unleached Al-$Zn_{0.20}Cd_{0.80}S$ has a type IV isotherm with a H3 type hysteresis loop that does not exhibit any limiting adsorption at high P/P_0. This is commonly observed with aggregates of plate like particles giving rise to slit-shaped pores [42], indicating that the plate like morphology of the LDHs precursor has been retained after sulfuration [43]. As expected, removal of the amorphous alumina leads to remarkable differences in the pore characteristics of the materials. Samples $Zn_{0.20}Cd_{0.80}S$-40 and $Zn_{0.20}Cd_{0.80}S$-50 have type IV isotherms with pronounced H2 type hysteresis loops, which are characteristic of mesoporous materials. The N_2 adsorption jump in the range $P/P_0 = 0.4$–0.9 is due to the capillary condensation in the mesopores [44]. The monotonic shift of the closure points to higher relative pressure in the isotherms of samples $Zn_{0.20}Cd_{0.80}S$-40 and $Zn_{0.20}Cd_{0.80}S$-50 is indicative of an increase in the pore diameter

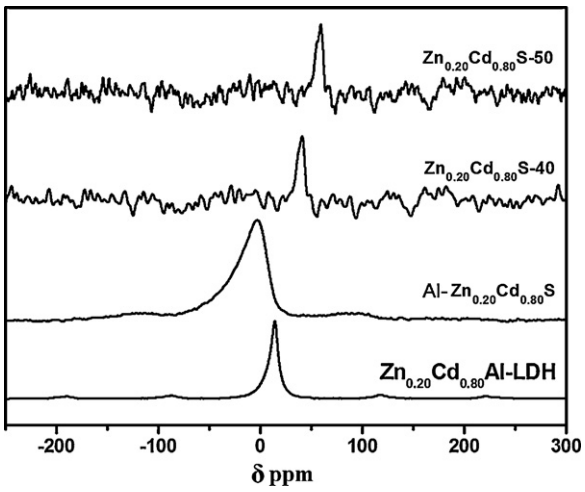

Fig. 8. ^{27}Al solid-state MAS NMR spectra of $Zn_{0.20}Cd_{0.80}$-LDHs precursor, unleached Al-$Zn_{0.20}Cd_{0.80}S$, and leached $Zn_{0.20}Cd_{0.80}S$-40 and $Zn_{0.20}Cd_{0.80}S$-50 sample.

of the samples. From the BJH pore size distributions (Fig. 9b), it can be observed that smaller diameter pores originally present in sample Al-$Zn_{0.20}Cd_{0.80}S$ disappear after removal of alumina and exhibit only a very narrow pore size distribution in the range below 40 nm. The large amount of amorphous alumina is very effective in separating the Al-$Zn_xCd_{1-x}S$ nanoparticles, and as a consequence of the resulting restricted the aggregation in the sulfuration

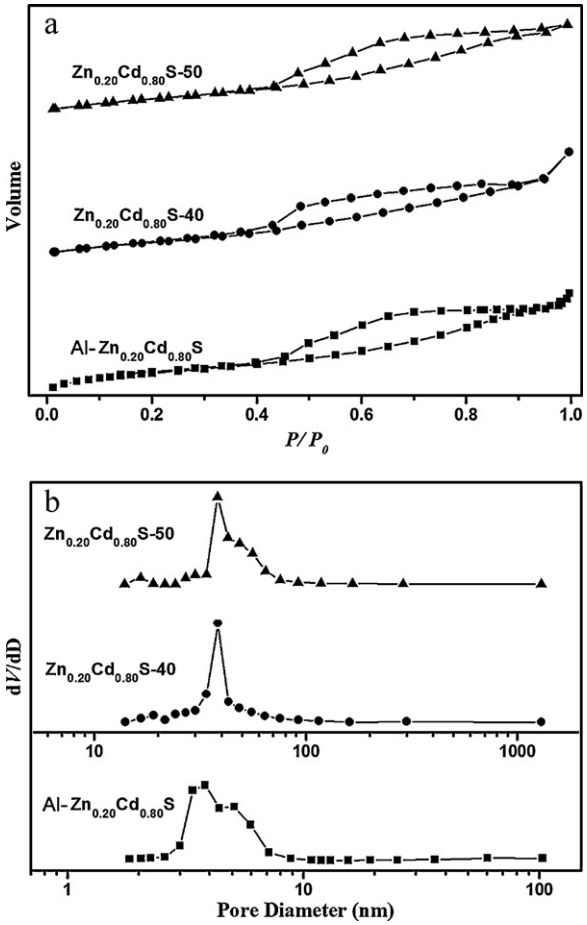

Fig. 9. N_2 adsorption isotherms (a) and pore size distributions (b) of $Zn_{0.20}Cd_{0.80}S$ before and after NaOH leaching.

Table 2
Textural properties of $Zn_{0.20}Cd_{0.80}S$ before and after NaOH leaching.

Sample	Surface area (m^2/g)[a]	Pore size (nm)[b]	Pore volume (cm^3/g)[b]
Al-$Zn_{0.20}Cd_{0.80}S$	8.17	4.69	0.089
$Zn_{0.20}Cd_{0.80}S$-40	28.5	37.99	0.094
$Zn_{0.20}Cd_{0.80}S$-50	33.9	38.02	0.095

[a] Surface area calculated from the N_2 adsorption isotherm according to the BET method.
[b] Pore size calculated from the N_2 desorption branch using the BJH model.

reaction, mesoporous $Zn_xCd_{1-x}S$ sample is obtained after removal of amorphous alumina.

As is shown in Table 2, the specific surface area and pore diameters of the leached samples increase with the increase of leaching temperature. As can be seen from the TEM image (Fig. 5), the mesoporous structure of the leached samples results mainly from the stack of $Zn_xCd_{1-x}S$ nanoparticles. Furthermore, it is also found that the total pore volume has little difference before and after leaching treatment and that a monomodal pore system (Fig. 9b) is formed after removal of the amorphous alumina, indicating that there may be a contraction of the mesoporous structure during alkali leaching process.

UV–vis absorption measurement is a convenient and effective method for investigating the band structures of semiconductors. By analysis of the absorption coefficients for $Zn_xCd_{1-x}S$ samples, the so-called optical energy gaps can be estimated using a classical Tauc approach [45,46]. Fig. 10 shows Tauc plots of $(\alpha E_p)^2$ *versus* E_p for three samples before and after NaOH leaching. It has been well established that, for a large number of semiconductors, the dependence of the absorption coefficient α, in the high-frequency region, on the photon energy E_p in optically-induced transitions, is given by the following expression:

$$\alpha E_p = K \cdot (E_p - E_g)^n \quad (1)$$

where E_g represents the optical band gap, K is a constant, and n depends on the nature of the transition—n has values of 1/2, 3/2, 2, and 3 for allowed direct transitions, forbidden direct transitions, allowed indirect transitions, and forbidden indirect transitions, respectively [47]. In the present case, the best fit of $(\alpha E_p)^2$ *versus* E_p was obtained for $n = 1/2$, suggesting there are allowed direct transitions across the energy band gap of the $Zn_xCd_{1-x}S$ solid solution. The extrapolated value (a straight line to the x-axis) of E_p at $\alpha = 0$ gives absorption edge energies corresponding to E_g. It is worth noting that the absorption edge of the samples extends increasingly into the visible region as the leaching temperature increasing: the

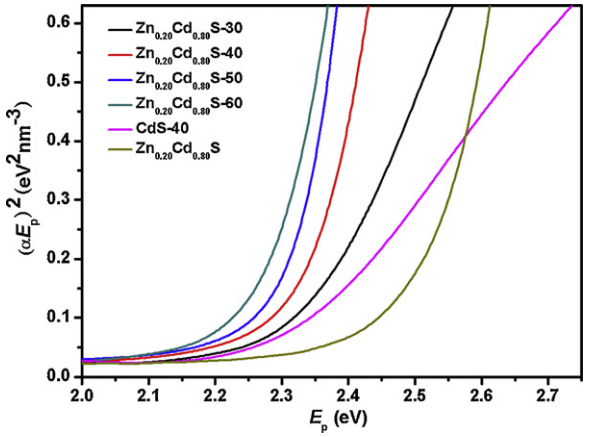

Fig. 10. Tauc plot for $Zn_{0.20}Cd_{0.80}S$ before and after NaOH leaching. (α represents the absorption coefficient and E_p the photon energy.).

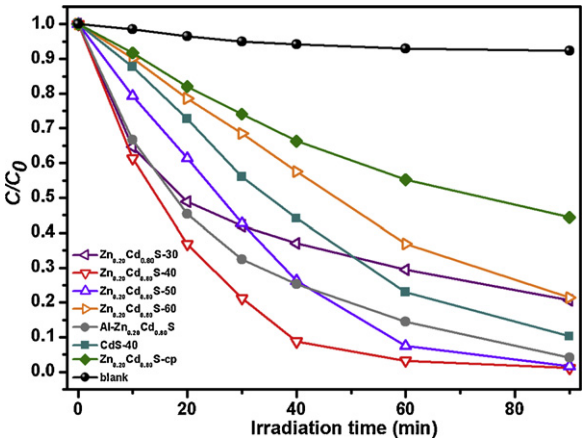

Fig. 11. Photodegradation of MB monitored as the normalized concentration change *versus* irradiation time.

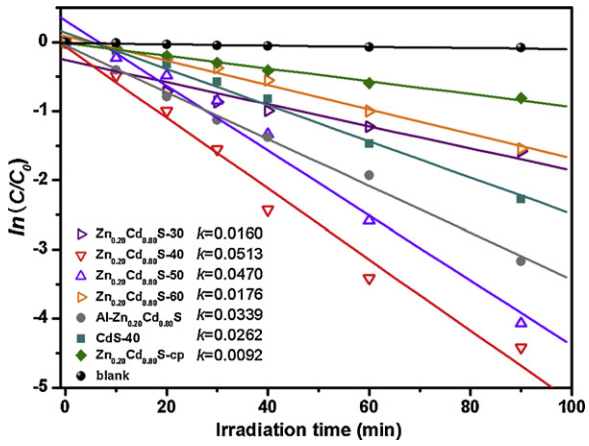

Fig. 12. First-order plots for the photodegradation of MB.

band gap energy decreases from 2.52 to 2.26 eV. The photogenerated electrons and holes migrate more convenient after removal of the optical inert amorphous alumina, suggesting the less residual alumina left the less band gap is. Compared to the $Zn_xCd_{1-x}S$-40 sample (2.34 eV), the band gap energy of CdS-40 (2.33 eV) was a little smaller because of not containing any Zn^{2+}.

Photocatalytic activities were evaluated for the samples before and after NaOH leaching under visible light irradiation, using the degradation of MB as a probe reaction. The adsorption–desorption equilibrium was established by stirring in the dark for 30 min before irradiation. The corresponding adsorption rate of all samples has been provided in Fig. S3, obviously, except the $Zn_{0.20}Cd_{0.80}S$-cp and the $Zn_xCd_{1-x}S$-60, the rest of the samples have a very low adsorption capacity after 90 min, indicating the influence of the adsorption capability of the samples on the MB photodegradation test can be ignored. In addition, the content of Na^+ in $Zn_xCd_{1-x}S$-40 was tested (showed in the Table S1), which indicates that the effect of Na^+ ion is also negligible. Fig. 11 shows the results for photodegradation of MB using the three solid solutions. As shown in Fig. 11, there is almost no degradation of the solution under visible light irradiation without any catalyst. It can be clearly seen that the photocatalytic conversion of MB with $Zn_{0.20}Cd_{0.80}S$-40 reached as high as 96% after 60 min of irradiation. For the samples at different leaching temperature, the photocatalytic activity showed as follows: $Zn_{0.20}Cd_{0.80}S$-40 > $Zn_{0.20}Cd_{0.80}S$-50 > $Zn_{0.20}Cd_{0.80}S$-30 > $Zn_{0.20}Cd_{0.80}S$-60, this means 40 °C is the optimal leaching temperature to improve the photocatalytic activity. The CdS-40 also showed lower photocatalytic activity than $Zn_{0.20}Cd_{0.80}S$-40 as no Zn^{2+} was contained. And, the photocatalytic activity of Al-$Zn_{0.20}Cd_{0.80}S$, $Zn_{0.20}Cd_{0.80}S$-40 and $Zn_{0.20}Cd_{0.80}S$-50 sample is much higher than that of $Zn_{0.20}Cd_{0.80}S$-cp sample obtained by the coprecipitation method with the same composition. For the $Zn_{0.20}Cd_{0.80}S$-40, the pH of the MB solution during the reaction process was monitored. The pH of original MB solution is 6.01, after adding the $Zn_{0.20}Cd_{0.80}S$-40 (which has been washed to pH 7 before dried) and magnetically stirred in the dark for 30 min, the pH of solution changed to 6.06, and the final pH of the solution we got after the photo-reaction is 6.67. These changes of pH also reflected that the MB was degraduated during the photo-reaction. The SEM and TEM images of the $Zn_{0.20}Cd_{0.80}S$-40 sample after the photo-reaction were showed in Fig. S4, the structure change of the $Zn_{0.20}Cd_{0.80}S$-40 sample is negligible, which means the catalyst keep stable during the reaction.

In the heterogeneous photocatalytic reaction, when the concentration of reactants is low, the photodegradation process generally obeys pseudo-first-order kinetics as shown by the linear plots of $\ln(C/C_0)$ *versus* irradiation time (t), and the reaction rate constant k can be obtained by calculating the slope. The kinetics of photodegradation process was investigated, and the results (Fig. 12) show that the photodegradation kinetics of MB on the photocatalysts mentioned above can fit the pseudo-first-order kinetics well, and all of the linear correlation coefficients R^2 are around 0.99. The rate constants of the $Zn_{0.20}Cd_{0.80}S$-40 and $Zn_{0.20}Cd_{0.80}S$-50 sample are 0.0513 and 0.0470 min^{-1}, respectively, and higher than that of the unleached sample. It is indicated that the removal of the amorphous alumina is beneficial to migration of the photogenerated electrons and holes, thereby, achieving the enhancement of the photocatalytic activity. Notably, the band gap of $Zn_{0.20}Cd_{0.80}S$-50 is less than that of $Zn_{0.20}Cd_{0.80}S$-40, while the photocatalytic activity of the former is lower than the latter. In our previous work, we have demonstrated that $Zn_xCd_{1-x}S$ solid solution showed a maximum in activity with an optimum Zn incorporation corresponding to $x \sim 0.2$. Meanwhile, the partial loss of Zn^{2+} at higher leaching temperature leads to the decline of the Zn/Cd molar ratio (Table 1). Therefore, the lower photocatalytic activity of $Zn_{0.20}Cd_{0.80}S$-50 than that of $Zn_{0.20}Cd_{0.80}S$-40 can be attributed to the decline of Zn/Cd molar ratio.

A recent solid-state multinuclear NMR study of LDHs [22] revealed that the metal cations adopt a highly ordered arrangement on an atomic level within the layers, where octahedral of M^{2+} and M^{3+} (six-fold coordinated to OH^-) share edges to form infinite sheets (Fig. 1) [26]. These sheets are stacked with each other and are held together by hydrogen bonding. The positive charge in the hydroxyl sheet is compensated by DS anions, which lie in the interlayer region between the two brucite-like sheets. In the subsequent sulfuration reaction, the divalent metal cations (Zn^{2+} and Cd^{2+}) react with gaseous H_2S to form sulfide solid solution. The surrounding Al^{3+}—O(H) octahedral migrate to form amorphous alumina with a large number of hydrogen bonding breaking up, and plays an important role in confining the growth of the nanoparticles. Because of the intercalated DS anions, the catalyst illustrated the short-range ordered structure. The alumina cannot be excited by UV or visible light, and hinders the migration of the photogenerated charge carriers in solid solution. As a consequence, selective leaching of alumina from the sulfuration product can be considered a promising method to further enhance the photocatalytic activity of the as-prepared. We can see that after the leaching process, the mesoporous is obtained, retaining regular arrangement to form the uniform distributed structure. Abundant dangling bonds and lattice defects (oxygen vacancies) can be generated, which are beneficial to formation of the hydroxyl groups and the adsorption of the O_2, respectively.

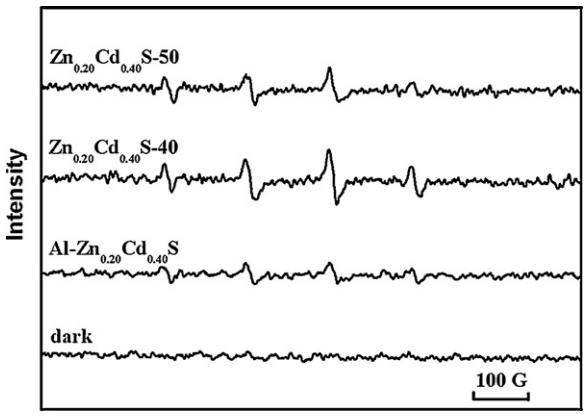

Fig. 13. ESR signals of the DMPO–•OH adducts formed in the suspensions of the Al-$Zn_{0.20}Cd_{0.80}S$, $Zn_{0.20}Cd_{0.80}S$-40 and $Zn_{0.20}Cd_{0.80}S$-50 sample before and after visible light irradiation.

Upon supra-band gap irradiation of particles the positive holes (h^+) are generated in the valence band, and the negative electrons (e^-) appear in the conduction band of a semiconductor as in Eq. (2) [1,48]:

$$+hv \rightarrow (e^- + h^+) \quad (2)$$

The photogenerated charge carriers may be involved in redox processes at the surface [1]. The positive h^+ are trapped by surface hydroxyl groups forming reactive hydroxyl radicals in aquatic media Eq. (3):(3)$OH^- + h^+ \rightarrow {}^\bullet OH$

In the aerated system, oxygen serves as a very effective electron acceptor producing super-oxide anion radicals, according to Eq. (4):(4)$O_2 + e^- \rightarrow O_2^{-\bullet}$

Usually, the increase of hydroxyl content on the surface of samples is beneficial to the enhancement of photocatalytic activity [1]. The surface-bound hydroxyl radicals (•OH) and super-oxide anion radicals ($O_2^{-\bullet}$) are important redoxinitiator for photocatalytic decomposition of the organic compound. Clearly, increased hydroxyl groups and adsorbed O_2 are favorable for the enhancement of photocatalytic activity. Therefore, compared with the unleached sample, the mesoporous $Zn_xCd_{1-x}S$ displays higher photocatalytic efficiency.

ESR spectroscopy has been frequently applied to investigate the initial steps of photocatalytic reactions at a molecular level. In particular, this technique has been used to follow the photoinduced generation of charge carriers on photocatalysts and their transfer to inorganic adsorbed molecules like O_2 and H_2O. The ESR spin-trap technique (with DMPO) was employed to probe the nature of the reactive oxygen species generated from $Zn_{0.20}Cd_{0.80}S$ samples before and after NaOH leaching under visible light irradiation. As shown in Fig. 13, the characteristic four peaks of DMPO–•OH with intensity 1:2:2:1 are observed, which is similar to the results reported by other groups for the •OH adduct [49,50], no such signals were detected in the dark. This means that irradiation is essential for generation of •OH on the surface of the catalyst. Furthermore, the peak intensity of •OH generated from the samples showed that $Zn_{0.20}Cd_{0.80}S$-40 > $Zn_{0.20}Cd_{0.80}S$-50 > Al-$Zn_{0.20}Cd_{0.80}S$. This is consistent with their photocatalytic performance: after irradiation for 90 min, the rate constants of the $Zn_{0.20}Cd_{0.80}S$-40 and $Zn_{0.20}Cd_{0.80}S$-50 were 0.0513 and 0.0470 min^{-1}, respectively, but only 0.0339 min^{-1} of the untreated Al-$Zn_{0.20}Cd_{0.80}S$ sample.

4. Conclusions

A series of mesoporous $Zn_xCd_{1-x}S$ nanoparticles with different molar ratios of Zn/Cd can be synthesized by a two-steps strategy: Al-$Zn_xCd_{1-x}S$ nanoparticles with homogeneously distributed structure was first synthesized by *in situ* gas–solid reaction of a single ZnCdAl-LDHs precursor with gaseous H_2S; subsequently, selective leaching of amorphous alumina by sodium hydroxide solution from the as-prepared Al-$Zn_xCd_{1-x}S$ nanoparticles was carried out, with the aim of achieving the introduction of mesopority in the chalcogenide semiconductor. The mesoporous $Zn_{0.20}Cd_{0.80}S$ nanoparticles can retain the uniform distributed structure with a network-like manner. The absorption edge of mesoporous $Zn_xCd_{1-x}S$ is monotonically blue shifted within the visible light region as the amount of residual alumina decreased. Mesoporous $Zn_xCd_{1-x}S$ samples exhibit higher photocatalytic activities for MB photodegradation under visible light illumination than the unleached Al-$Zn_xCd_{1-x}S$ and $Zn_xCd_{1-x}S$-cp sample prepared by the coprecipitation method with the same composition. The abundance of hydroxyl groups on the surface of mesoporous $Zn_xCd_{1-x}S$ solid solution after the selective leaching of alumina and the high surface areas are proposed to lead to improved photocatalytic activity.

Acknowledgments

We acknowledge generous financial support from the National Natural Science Foundation of China and the 973 Program (no. 2011CBA00506).

Appendix A. Supplementary data

Supplementary data associated with this article can be found, in the online version, at http://dx.doi.org/10.1016/j.apcatb.2012.05.018.

References

[1] M.R. Hoffmann, S.T. Martin, W. Choi, D.W. Bahnemann, Chemical Reviews 95 (1995) 69–96.
[2] M. Anpo, M. Takeuchi, Journal of Catalysis 216 (2003) 505–516.
[3] M. Grätzel, Nature 414 (2001) 338–344.
[4] J.H. Pan, H.Q. Dou, Z.G. Xiong, C. Xu, J.Z. Ma, X.S. Zhao, Journal of Materials Chemistry 20 (2010) 4512–4528.
[5] B.Z. Tian, X.Y. Liu, L.A. Solovyov, Z. Liu, H.F. Yang, Z.D. Zhang, S.H. Xie, F.Q. Zhang, B. Tu, C.Z. Yu, O. Terasaki, D.Y. Zhao, Journal of the American Chemical Society 126 (2004) 865–875.
[6] G.J. de, A.A. Soler-Illia, C. Sanchez, B. Lebeau, J. Patarin, Chemical Reviews 102 (2002) 4093–4138.
[7] W.S. Chae, H.W. Shin, E.S. Lee, Y.R. Kim, Chemistry of Materials 17 (2005) 3072–3074.
[8] G. Lin, J. Zheng, R. Xu, Journal of Physical Chemistry C 112 (2008) 7363–7369.
[9] B. Liu, C.Z. Hua, Journal of the American Chemical Society 126 (2004) 16744–16746.
[10] H.G. Yang, H.C. Zeng, Angewandte Chemie International Edition 43 (2004) 5206–5209.
[11] J.H. Pan, X. Zhang, A.J. Du, D.D. Sun, J.O. Leckie, Journal of the American Chemical Society 130 (2008) 11256–11257.
[12] D.V. Bavykin, V.N. Parmon, A.A. Lapkin, F.C. Walsh, Journal of Materials Chemistry 14 (2004) 3370–3377.
[13] J. Cheon, J.I. Zink, Journal of the American Chemical Society 119 (1997) 3838–3839.
[14] X.H. Zhong, Y.Y. Feng, W. Knoll, M.Y. Han, Journal of the American Chemical Society 125 (2003) 13559–13563.
[15] W.Z. Wang, I. Germanenko, M.S. El-Shall, Chemistry of Materials 14 (2002) 3028–3033.
[16] J.G. Yu, J. Zhang, M. Jaroniec, Green Chemistry 12 (2010) 1611–1614.
[17] J. Zhang, S.W. Liu, J.G. Yu, M. Jaroniec, Journal of Materials Chemistry 21 (2011) 14655–14662.
[18] W.J. Li, D.Z. Li, Z.X. Chen, H.J. Huang, M. Sun, Y.H. He, X.Z. Fu, Journal of Physical Chemistry C 112 (2008) 14943–14947.
[19] C.J. Xing, Y.J. Zhang, W. Yan, L.J. Guo, International Journal of Hydrogen Energy 31 (2006) 2018–2024.
[20] W.Z. Wang, W. Zhu, H.L. Xu, Journal of Physical Chemistry C 112 (2008) 16754–16758.
[21] X. Xu, R.J. Lu, X.F. Zhao, S.L. Xu, X.D. Lei, F.Z. Zhang, D.G. Evans, Applied Catalysis B 102 (2011) 147–165.
[22] P.J. Sideris, U.G. Nielsen, Z.H. Gan, C.P. Grey, Science 321 (2008) 113–117.
[23] V. Rives, Layered Double Hydroxides: Present and Future, Nova Science Publishers, New York, 2001.

[24] P.S. Braterman, Z.P. Xu, F. Yarberry, in: S.M. Auerbach, K.A. Carrado, P.K. Dutta (Eds.), Handbook of Layered Materials, Marcel Dekker, Inc., New York, 2004, p. 373.
[25] G.R. Williams, D. O'Hare, Journal of Materials Chemistry 16 (2006) 3065–3074.
[26] F. Cavani, F. Trifiró, A. Vaccari, Catalysis Today 11 (1991) 173–301.
[27] J.K. Furdyna, Journal of Applied Physics 64 (1988) 3663–3664.
[28] I. Tsuji, H. Kato, H. Kobayashi, A. Kudo, Journal of the American Chemical Society 126 (2004) 13406–13413.
[29] Z. An, J. He, X. Shu, Y.X. Wu, Chemical Communications 9 (2009) 1055–1057.
[30] F. Jiao, A.H. Hill, A. Harrison, A. Berko, A.V. Chadwick, P.G. Bruce, Journal of the American Chemical Society 130 (2008) 5262–5266.
[31] P.F. Ji, J.L. Zhang, F. Chen, M. Anpo, Journal of Physical Chemistry C 112 (2008) 17809–17813.
[32] S.F. Wang, F. Gu, C.Z. Li, M.K. Lü, Crystal Growth and Design 7 (2007) 2670–2674.
[33] S.E. Skrabalak, K.S. Suslick, Journal of the American Chemical Society 127 (2005) 9990–9991.
[34] K. Zhang, D.W. Jing, Q.Y. Chen, L.J. Guo, International Journal of Hydrogen Energy 35 (2010) 2048–2057.
[35] A. Deshpande, P. Shah, R.S. Gholap, N.M. Gupta, Journal of Colloid and Interface Science 333 (2009) 263–268.
[36] S. Celebi, A.K. Erdamar, A. Sennaroglu, A. Kurt, H.Y. Acar, Journal of Physical Chemistry B 111 (2007) 12668–12675.
[37] S.W. Lu, H.K. Schmidt, Materials Research Bulletin 43 (2008) 583–589.
[38] J.C. Yu, J.G. Yu, J.C. Zhao, Applied Catalysis B 36 (2002) 31–43.
[39] J. Yu, X. Zhao, Materials Research Bulletin 36 (2001) 97.
[40] M.R. Weir, R.A. Kydd, Inorganic Chemistry 37 (1998) 5619–5624.
[41] S.J. Miao, N.A. Raoul, R. Thomas, K. Igor, B. Malte, S. Robert, M. Martin, European Journal of Inorganic Chemistry 7 (2009) 910–921.
[42] K.S.W. Sing, D.H. Everett, R.A.W. Haul, L. Moscou, R.A. Pierotyi, J. Rouquérol, T. Siemieniewska, Pure and Applied Chemistry 57 (1985) 603–619.
[43] W.T. Reichle, S.Y. Kang, D.S. Everhardt, Journal of Catalysis 101 (1986) 352–359.
[44] L. Zou, F. Li, X. Xiang, D.G. Evans, X. Duan, Chemistry of Materials 18 (2006) 5852–5859.
[45] D.F. Wang, T. Kako, J.H. Ye, Journal of the American Chemical Society 130 (2008) 2724–2725.
[46] A. Ishikawa, T. Takata, J.N. Kondo, M. Hara, H. Kobayashi, K. Domen, Journal of the American Chemical Society 124 (2002) 13547–13553.
[47] L. Zou, X. Xiang, J. Fan, F. Li, Chemistry of Materials 19 (2007) 6518–6527.
[48] D. Dvoranová, V. Brezová, M. Mazúr, M.A. Malati, Applied Catalysis B 37 (2002) 91–105.
[49] W. Zhao, W.H. Ma, C.C. Chen, J.C. Zhao, Z.G. Shuai, Journal of the American Chemical Society 126 (2004) 4782–4783.
[50] T. Yamaki, T. Umebayashi, T. Sumita, S. Yamamoto, M. Maekawa, A. Kawasuso, H. Itoh, Nuclear Instruments and Methods in Physics Research: Section B 206 (2003) 254–258.